Journal of Materials Research and Technology 30 (2024) 3238–3250

Contents lists available at ScienceDirect

Journal of Materials Research and Technology

journal homepage: www.elsevier.com/locate/jmrt

Coupling μ-computed tomography and multi-scale modelling to assess the mechanical performance of material extrusion metal components

L.M. Cacho *, M.A. Neto, D.M. Neto, M.T. Vieira

CEMMPRE, ARISE, Department of Mechanical Engineering, University of Coimbra, Polo II, Rua Luís Reis Santos, Pinhal de Marrocos, 3030-788, Coimbra, Portugal

ARTICLE INFO

Keywords:
Metal additive manufacturing
Material extrusion
Micro computed tomography
Porosity
Finite element analysis

ABSTRACT

The porosity defects arising in objects produced by metal Material Extrusion (MEX) additive manufacturing affect the macroscopic mechanical behaviour. This paper presents a new approach integrating μ-computed tomography (μXCT) and multi-scale finite element analysis to evaluate the mechanical performance of components fabricated by metal MEX. The porosity information from μXCT is mapped into the finite element model, allowing to define the volume fraction of porosity to each finite mesh element. Then, the Mori-Tanaka homogenization technique is used to estimate the effective mechanical properties in each integration point, assuming a representative volume element composed by a metal matrix with a void. The reliability of the proposed approach was assessed using tensile specimens of stainless steel 316L produced by metal MEX. The numerical predictions were compared with experimental measurements, namely the strain field evolution measured by digital image correlation (DIC). The results highlight the detrimental influence of the porosity distribution, evaluated in the specimen using μXCT, on the strain distribution during the loading stage. The numerical predictions are in agreement with the experimental measurements, i.e. the difference is lower than 11%. Therefore, the proposed approach offers valuable insights for evaluating the mechanical performance of components produced by metal MEX, focusing on the detrimental effects of porosity defects.

1. Introduction

The international standard establishes and defines Material Extrusion (MEX) as the Additive Manufacturing process (AM) in which material is selectively dispensed through a nozzle orifice [1]. The printed material is deposited in the printing heated bed following a specific pattern derived from a CAD model, enabling the construction of the 3D object in a layer-by-layer configuration [2]. In case of MEX of metals, the feedstock comprises metal powder particles, polymeric binders and additives [3]. This multi-material formulation is heated until it's softened and has the condition to be extruded thru the nozzle. The multi-step process requires two additional phases besides the shaping: the debinding phase to remove the binder and the sintering to consolidate the metal particles into the final metal component [4]. MEX experienced rapid growth thanks to the process's low shaping set-up and running cost, the wide selection of printing materials available, and the existing knowledge of extrusion-based processes [5]. However, some drawbacks still prevent its widespread implementation, namely the presence of random intrinsic defects. MEX components display different microstructural defects (pores) with different origins and impacts on the final object. Imprecise control of the debinding stage can lead to the formation of large internal voids due to insufficient gas flow rate or to the stresses applied by the gas trying to flow out of the parts [6–8]. On the other hand, inaccurate shaping, slicing parameters and filament diameter variation lead to the formation of spaces between printed strands. Even with the anisotropic shrinkage, these void spaces are always transported to the final metal part originating chain of pores, most of them with an elongated shape [9–11]. Sintering defects are temperature-related and impossible to remove in totality, as it is impossible to achieve perfect density in the thermal sintering process [12].

The presence of unknown physical defects in the interior of structural components can have a detrimental effect on the component's mechanical strength. In the case of components subjected to cyclic loads, the impact of having interior porosity is even more prejudicial because the fatigue life can be strongly reduced [13,14]. Carlton et al. [15] reported that the failure in uniaxial tensile specimens presenting porosity is highly defect-driven. Nevertheless, other studies have adopted the

* Corresponding author.
E-mail addresses: luis.cacho@dem.uc.pt (L.M. Cacho), augusta.neto@dem.uc.pt (M.A. Neto), diogo.neto@dem.uc.pt (D.M. Neto), teresa.vieira@dem.uc.pt (M.T. Vieira).

https://doi.org/10.1016/j.jmrt.2024.04.065
Received 29 December 2023; Received in revised form 5 April 2024; Accepted 8 April 2024
Available online 9 April 2024

defect-tolerant design for Metal Additive Manufacturing (MAM) components, where existing internal physical defects are considered during the design stage [16]. Several research works have clearly pointed out the need to identify, measure, and analyse the impact of these defects on the final mechanical performance [17,18]. Hence, the rejection of components with defects can be avoided if their impact on the mechanical behaviour is known a priory, allowing to lower the waste associated with the production. Despite all research efforts, MAM processes have still not been used to produce structural components to a significant extent. Indeed, the qualification of MAM components is relatively recent, requiring significant empirical testing [19]. The establishment of comprehensive, widely accepted standards to certify MAM components is still under development [20,21].

The porosity in the parts produced by MAM can be evaluated by different techniques, which can be divided into two groups: destructive and non-destructive. Metallographic image analysis allows for the identification and quantification of porosity in a predefined cross-section but requires the cutting of the part or specimen [22]. The most common non-destructive techniques for porosity analysis are ultrasonic testing, X-ray inspection and Archimedes density characterization. Nevertheless, these techniques are unable to provide detailed information about the porosity present in the interior of a component. Indeed, the Archimedes density analysis only provides information about the volume, being inadequate to provide information about size, location, morphology and distribution of the porosity [18]. On the other hand, X-ray inspection only gives information on the 2D plane [23], and ultrasonic testing is dependent on the geometry being analysed and has difficulties detecting small pores when compared with novel techniques [24]. The emergence of micro X-ray computed microtomography (μXCT) allowed us to perform quantitative volumetric inspections and measurements of complex internal features, such as defects, without destroying the part [25]. Liverani et al. [26] used the μXCT technique to establish a correlation between the laser-powder bed fusion parameters and the resulting density of the specimens of AISI 420. The μXCT technique has also been used to study the formation and evolution of sintering defects, the damage evolution and failure mechanisms in MAM specimens [15,27]. Although the huge potential of the μXCT technique, the final 3D object density and the consequent detection of defects are strongly affected by the segmentation methods and the threshold resolution of the scan [28,29].

Several modelling techniques have been recently developed to predict manufacturing defects, including porosity formation [30]. However, the actual physics-based models are limited to meso-scale analysis due to the complex multi-physics phenomena involved in the MAM process [31]. Besides, the adoption of multi-scale approaches requires a prohibitive computation time. Alternatively, the numerical simulation can be used to evaluate the mechanical response of the components produced by MAM. Accordingly, the internal porosity is generally neglected, i.e., the material is assumed to be continuous and homogeneous (defect free). Nevertheless, integrating the data from μXCT into the finite element (FE) analysis can help assess the impact of the intrinsic physical defects on the structural performance. Hardin et al. [23] pointed out very early the importance of this connection, developing a method to transfer the porosity distribution, measured from 2D radiographs, into the finite element analysis. Considering a distributed initial porosity, they used the Gurson-Tvergaard-Needleman damage material model in the non-linear finite element analysis. Siddique et al. [32] explored an identical approach, connecting the data obtained from μXCT to the finite element analysis. The 3D geometry of the component was reconstructed, meshed and then exported to the Abaqus finite element solver; nevertheless, they needed to de-select smaller pores for simplification. Other research studies using segmented 3D digital images [33] with a costume-developed model, and Volume Graphics software [34] showed good promise in performing structural analysis using the μXCT data. Still, they can only assess the material linear response. Most studies are based on single pore models with linear or non-linear material behaviour. Continuum material models are used to define an initial fraction of porosity homogeneously distributed in a specimen or representative volume element. However, in the case of MAM processes, the porosity volume fraction cannot be assumed either homogeneously or isotropic to represent the whole 3D object [35–39].

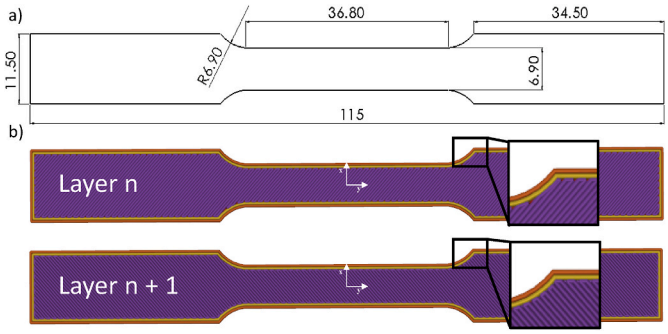

Fig. 1. Specimen produced by MEX: (a) Geometry and main dimentions in mm (pre sintering); (b) Printing strategy of two sequential layers N and N+1 with rectilinear infill pattern.

The main objective of this study was to create a simple and viable way of communication between FE analysis and μXCT data, capable of qualifying the random and intrinsic microstructural defects (pores) on MAM components. The proposed method uses a mean-field homogenization method to define the mechanical behaviour of each finite element in the mesh, depending on the defects detected in the μXCT dimensional analysis. The paper is divided into four main sections. The present section is the first and synthesizes the MAM issues; section 2 contains the physical experimental procedure concerning the production of 3D objects by MAM, the porosity evaluation and mechanical testing. Section 3 comprises the procedure related to the numerical model: defects mapping, FE boundary conditions to the constitutive material model and homogenization theory used. The results and discussion are presented in section 4. This section evaluates and measures results from the uniaxial tensile test and builds a strong relationship between numerical and experimental data. The main conclusions are presented in section 5.

2. Experimental procedure

2.1. Samples fabricated by MEX

The preparation of the feedstock and filament was carried out according to the procedure proposed by Cerejo et al. [40]. The stainless steel 316 low carbon nitrogen-atomized powder (Osprey Sandvik®), with particle size d_{90} = 10 μm and shape factor of 1, was used. The SS316L powder was mixed with the master binder (M1) and additives (TPE and plasticizer) in a Plastograph Brabender W50 (Brabender GmbH & co. KG, Duisburg, Germany). SS316L powder particles represented 60% of the feedstock volume, while the M1, TPE and additives volume fractions were 30%, 7% and 3%, respectively. The mixing chamber temperature was 180 °C, and the blade rotation speed was 30 rpm. The mixing operation was performed during a time required to reach a homogeneous mixture dictated by a steady state regime in the magnitude of the applied torque. The resulting feedstock was cut into small pellets and extruded into filament form. The filament was fabricated in a single screw extruder (Brabender GmbH & Co., Duisburg, Germany), which presents five heating zones (160 °C, 165 °C, 170 °C, 175 °C and 180 °C) along the screw direction and 1.75 mm of nozzle diameter. The cross-section of the produced filament was measured to evaluate the dimensional accuracy, which was 1.75 ± 0.05 mm.

The flat dogbone-shaped tensile specimen was produced by MEX, allowing the subsequent evaluation of the mechanical strength. The final dimensions of objects produced by MEX are influenced by the shrinkage occurring during the debinding and sintering stage [41]. Hence, the

Table 1
Print parameters selected in PrusaSlicer 2.4.0 to fabricate the flat dogbone-shaped tensile specimen.

Printing parameter	Value
Nozzle temperature [°C]	190
Build platform temperature [°C]	60
Nozzle diameter [mm]	0.4
Layer thickness [mm]	0.2
Printing speed [mm/s]	25
Fill pattern (100% infill)	rectilinear
Number of perimeters	2

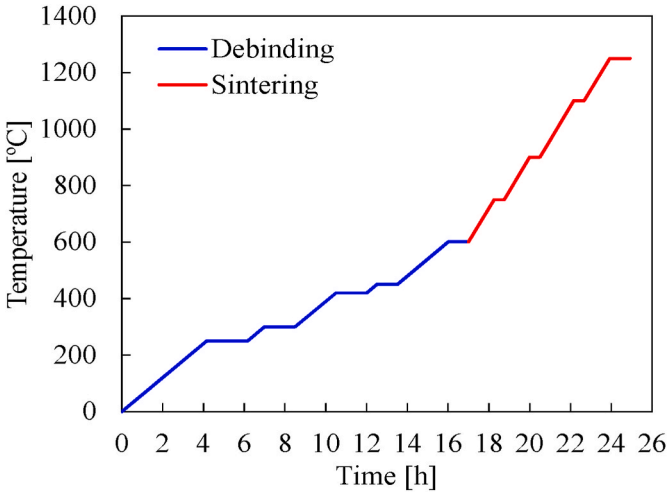

Fig. 2. Debinding and sintering cycle applied to the specimens.

desired size of the samples was defined according to the "ASTM E8/E8M standard for tension testing of metallic materials" and were scaled in all directions to produce the geometry of the green part [42]. Previous studies on the same material showed that the shrinkage is approximately 15% in the xy plane and 25% along the z-axis (thickness of the specimens) [43]. Thus, the scale factor applied to the desired geometry was 1.15, 1.15 and 1.25 in the x, y and z directions, respectively, as shown in Fig. 1 (a). The thickness of the shaping scaled object is 2.5 mm. The G-code containing the printing strategy (Fig. 1 (b)) was generated in the PrusaSlicer 2.4.0 and the specimens were printed in a Prusa MK3S using the parameters listed in Table 1. Since the diameter of the filament presents some variation along the length, the Repetier-Host was used to control printing parameters in real-time, namely the extrusion multiplier, allowing to reduce the possibility of having pores along the strand printed line. A total number of three specimens were produced under identical conditions.

The debinding and sintering stages were performed in a Termolab Sintering oven with an Argon atmosphere. The temperature evolution is presented in Fig. 2, which is usually adopted for the binder and additives used in the present study. The debinding operation shows five heating stages (1 °C/min) and five different holding stages to guarantee the proper elimination of organic constituents, requiring 17 h up to 600 °C. On the other hand, the sintering operation presents four heating stages (2 °C/min) and four different holding stages, requiring 7 h and 55 min for heating up to 1250 °C. The specimens were polished after sintering to reduce top layer surface roughness which was induced by the extrusion multiplier parameter. Besides, specimens were submitted to a heat treatment for residual stress relief, where the heating rate was 10 °C/min up to 450 °C with a dwell time of 1 h and left to cool inside the same oven.

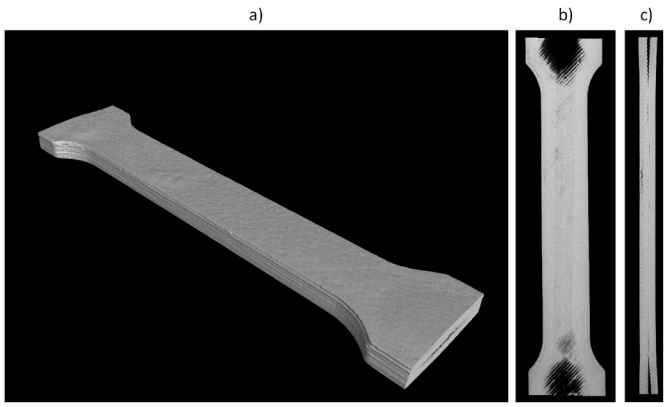

Fig. 3. μXCT reconstructed 3D object: a) perspective view of the specimen; b) section cut view of a plan parallel to the top face representing the middle of the specimen; c) section cut view of a plan parallel to the side face of the gauge length representing the middle of the specimen.

2.2. Tomography analysis

The internal porosity present in the sample fabricated by MEX was evaluated using μXCT analysis, allowing the accurate measurement of the size and location of the pores after debinding and sintering. Only a single specimen was analysed, which will be posteriorly used to assign the porosity volume fraction in the numerical model. The tomograph Nikon XTH 225 ST with a detector Varex 4343 CT, with a static target reflection and a minimum spot size of 3 μm, was used. The experimental analysis was performed using a voltage of 225 kV and 84 μA of current, with an angular step of 0.33° through 360° of rotation, with a voxel size of 19 μm. The 4448 series of sequential X-ray high-resolution images was coupled to generate the object's volume. The 3D geometry of the specimen was reconstructed using CT Pro 3D (Nikon Metrology) software and is presented in the Fig. 3.

Volume Graphics 2022.3 software was used to perform the porosity dimensional analysis on the scanned specimen. The outer surface of the 3D object was evaluated, and the pore detection was performed using VGDefX algorithm with void analysis. This analysis was carried out with an auto threshold deviation mode with a −0.75 deviation factor. The volumetric geometry of the specimen, delimited by the outer surface, was defined by a finite element mesh of tetrahedral elements generated in the Volume Graphics. The mesh's biggest and smallest element size was set to 0.1 mm, allowing an accurate discretization of the 3D object volume. After discretization, the void analysis was superposed on the mesh to assess the element porosity information. The result was a finite element mesh defining the geometry under analysis, containing the porosity volume fraction assigned to each finite element. Surface defects are not considered as pores by the transfer of data, so only internal geometry features were mapped.

2.3. Uniaxial tensile test

The mechanical strength of the samples fabricated by MEX was evaluated using the uniaxial tensile test, allowing to characterize both the elastic and the plastic behaviour under monotonic load. The nominal width and length of the parallel gauge section are 6.3 mm and 33 mm, respectively. The uniaxial tensile tests were carried out according to ASTM E8 standard [42] at room temperature using a universal tensile test machine Shimadzu Autograph AG-X universal testing machine equipped with a 10 kN load cell was used. The tests were performed until rupture under displacement control with prescribed crosshead velocity of 0.0167 mm/s.

The specimen strain field was measured using the VIC-3D Correlated Solutions ® (Correlated Solutions, Columbia, SC, USA) equipment, ensuring that both equipment was synchronized, i.e., the VIC-3D and the

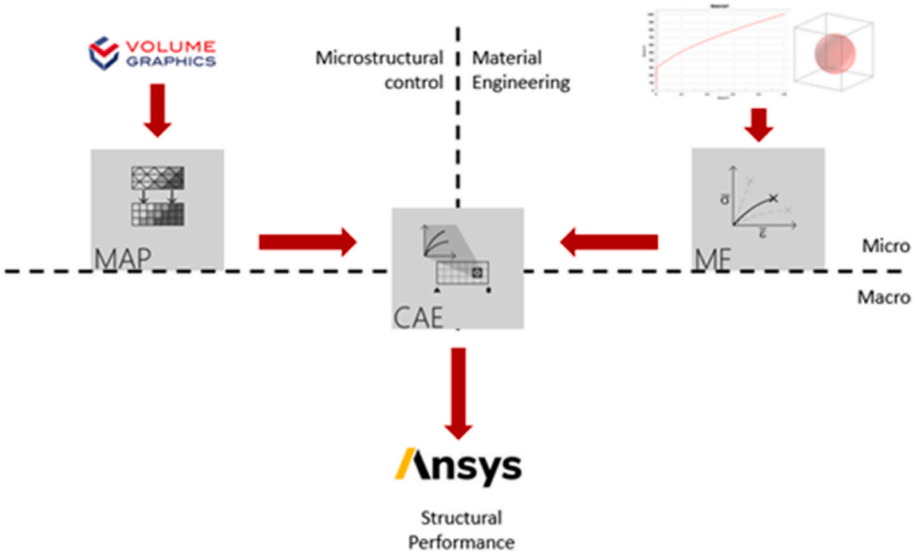

Fig. 4. Methodology flowchart - Integration of softwares.

tensile test machine. The use of DIC technique in several MAM studies reveals that during the tensile specimens the strain concentration is affected mainly by the internal pores [10,44]. This technique allows the evaluation of the heterogeneous strain distribution in the specimen gauge area (inhomogeneous material behaviour), resulting from the physical defects in the specimen's interior. The set-up comprises two stereo high-speed cameras (Stingray F–504B ASG, Allied Vision) equipped with two 75 mm focal length lenses (FL-CC7528-2 M, Ricoh Pentax), which were placed perpendicularly to the specimen surface with the airbrush-painted speckle pattern. Captured speckle images were analysed using the system VIC-3D 2012 recording the motion of the specimen surface at the acquisition frequency of 2 Hz. The lower face of the specimen (during the shaping stage) was selected to evaluate the strain field due to its flatness compared with the opposite face. The resolution was approximately 2 μm/pixel (2358 × 1728 pixels in the measurement area of 80 × 55 mm^2).

3. Numerical model

The methodology presented in this study, graphically described in Fig. 4, consists of the interoperability of two commercially available softwares with distinct applications. Digimat state-of-the-art material engineering capabilities intertwined with the ANSYS workbench for static finite element analysis to study the impact of the manufacturing final microstructure in the overall structural performance of MAM components. The Digimat (version 2022.2) platform employs a procedure with three main internal modules: Digimat-CAE establishes a hybrid connection using multi-scale coupling technique; Digimat-MAP transfers the microstructural data processed in the Volume Graphics to the ANSYS static structural mesh elements; Digimat-MF makes use of fast homogenization methods to give average responses of strain and stresses of the elements' macro material properties considering its micro constituents (metal matrix and void). The multi-scale coupling pre-computes the macroscopic material properties needed in the Ansys/Digimat-CAE communication interface (dynamic libraries) at each finite element mesh integration point. Hence, the hybrid parameters are computed from N number of Digimat-MF simulations. N is related to the number of groups of elements with different porosity volume fraction assignments after the mapping. Basically, the pre-processing step is equivalent to launching an extensive campaign of experimental tests with various porosity volume fractions. A microscopic model is defined for each porosity volume fraction, and the elastoplastic properties are calculated. To simulate the specimen's non-linear macroscopic mechanical response, static structural analysis was used in the workbench module in ANSYS software (version 2021 R2).

3.1. Geometry and boundary conditions

Only the gauge section of the uniaxial tensile test was modelled in order to reduce the computational effort. Considering the anisotropic shrinkage that occurred during the debinding and sintering stages, assuring that the areas with the highest interest are included in the numerical analysis, the dimensions of the specimen used in the numerical model were updated according to the experimental measurements of the specimen after debinding and sintering stages. Hence, the gauge section width, length and thickness were 6.3 mm, 33 mm and 2.08 mm, respectively. This paralelepipedal geometry was discretized with 436,590 linear hexahedral finite elements, corresponding to 0.1 mm of element size in all directions. Despite the apparent symmetry of the geometry, loading/boundary conditions and material isotropy, the inhomogeneous porous distribution requires the modelling of the entire specimen geometry.

The prescribed displacement (4 mm) was assigned to the nodes in one end face of the specimen, while the nodes located in the opposite extremity were constrained in the normal direction, i.e., in the loading direction. Additionally, a single node of the face constrained in the normal direction was fixed in all directions to prevent rigid body motion. The loading conditions were applied using 100 steps, i.e. the increment of prescribed displacement was 0.04 mm.

3.2. Material constitutive model

The Hooke's law defines the material mechanical behaviour in the linear elastic regime. Hence, the elastic properties considered for the SS316L were 200 GPa for the Young modulus and 0.28 for the Poisson ratio.

The elastoplastic constitutive model adopted in the present finite element model considers the plastic behaviour defined by: (i) isotropic yield criterion; (ii) isotropic hardening law and (iii) associated flow rule. The isotropic plastic behaviour was described by the von Mises isotropic yield criterion. The evolution of the flow stress with plastic strain was defined by the isotropic work hardening law:

$$Y = Y_0 + k\bar{\varepsilon}^p + R_\infty\{1 - \exp(-m\bar{\varepsilon}^p)\}, \quad (1)$$

where $\bar{\varepsilon}^p$ denotes the equivalent plastic strain, Y_0 is the initial yield

Table 2
Material Parameters used in the hardening law to describe the study SS316L.

Parameter	Y_0 [MPa]	k [MPa]	R_∞ [MPa]	m
Value	300	1035.44	202	8.3

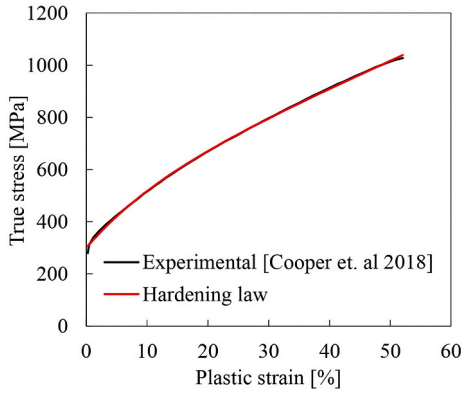

Fig. 5. Comparison between experimental and numerical true stress-strain of the forged SS316L tensile specimens [46].

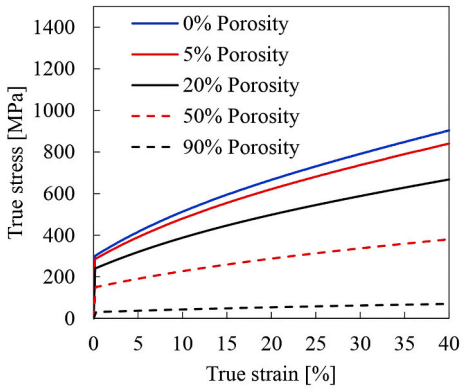

Fig. 6. Mori-Tanaka Homogenization: Variation of elastoplastic material properties with volume fraction of porosity.

stress. This exponential and linear law comprises three material parameters (Digimat version 2022.2): k represents the linear hardening modulus, R_∞ defines the hardening modulus and, lastly, the hardening exponent is defined by m [45].

The material parameters required to the numerical model were calibrated from the experimental stress–strain curve obtained by Cooper et al. [46] using forged SS316L tensile specimens. The procedure is based on the minimization the difference between the numerical and the experimental stress values [47]. The material parameters listed in Table 2 were obtained for the isotropic hardening law, Eq. (1). Fig. 5 presents the both the experimental and the numerical stress–strain curves. The numerical results are in good agreement with the experimental ones, i.e. the mechanical behaviour of this alloy is accurately described by this hardening law. It is important to note that the elastoplastic constitutive model cannot assess the impact of the nucleated or coalesced porosity that are the cause of fracture/ductile damage of metallic materials.

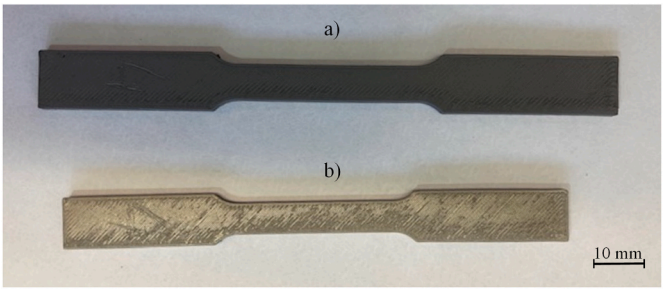

Fig. 7. Specimen geometry: a) before debinding and sintering (green specimen); b) after debinding and sintering (metal specimen). (For interpretation of the references to colour in this figure legend, the reader is referred to the Web version of this article.)

3.3. Homogenization procedure

The Mori-Tanaka (M-T) homogenization procedure was adopted in the present study to consider the effect of the physical porosity on the mechanical material response [48]. In this specific case, the material is defined by two phases: a metal material matrix and a single spherical pore with a shape factor of 1. The volume fraction of each phase is defined via the representative volume element (RVE) in each integration point of the finite element mesh. The mechanical properties are pre-computed and assigned to finite elements based on the porosity distribution. Fig. 6 presents the mechanical response (elastoplastic behaviour) resulting from the M-T homogenization model for different values of porosity volume fraction.

M-T model consists of a semi-analytical model that gives approximations to the volume averages of stresses and strains, either at the macro level or within each phase. The model is very successful in predicting the effective properties of two-phase materials; in theory, it is restricted to a moderate volume fraction of inclusions (less than 25%), but can give good approximations in all ranges [49,50].

3.4. Porosity mapping

The finite element mesh adopted in the non-linear finite element analysis is composed of linear hexahedral finite elements (see Section 3.1). Notice that the specimen's geometry resulting from the μXCT analysis is defined by tetrahedral finite elements (see Section 2.2) and, therefore, the porosity volume fraction is assigned to each tetrahedron element. Hence, a mapping procedure is required to transfer the porosity volume fraction from the tetrahedral finite elements mesh (donor) to the hexahedral mesh (receiver). Moreover, these two mesh geometries are not precisely identical since the numerical analysis was carried out considering the nominal dimensions of the specimen (only the parallel gauge section), while the μXCT analysis provides realistic geometry and dimensions. Previous literature studies have used a mapping procedure to transfer input damage [51], porosity volume fraction [52], fibre orientation [53] and residual stress information [54] to the simulation meshes.

The Digimat-MAP module was used for mapping the porosity volume fraction between dissimilar meshes, considering two different mapping methods: (i) element to integration point (ELE2INT) and (ii) integration point/node to integration point (INT-NODE2INT) [45]. The second method is the Digimat default mapping algorithm. In this method, the integration points of the hexahedral receiving mesh (8 integration points) are localized in the tetrahedral donor mesh (1 integration point). Data is mapped from the donor mesh nodes to the receiver mesh's integration points. There is a natural occurrence of smoothing. Using the ELE2INT method there is no interpolation, the integration points of the receiving mesh are located in the donor mesh and then the data values of the finite elements of the donor mesh are directly transferred to the receiving mesh integration point. Before the application of the mapping procedure, it is necessary to guarantee that both meshes have identical spatial locations. Thus, an automatic superposition transformation was adopted, considering a tolerance of 0.2 mm. After the method of automatic superposition is applied, the data is mapped from the donor mesh to the receiver mesh.

Table 3
Shrinkage of the specimens (3 samples) after debinding and sintering.

	X Shrinkage [%]	Y Shrinkage [%]	Z Shrinkage [%]
Sample 1	14.4	14.2	17.6
Sample 2	14.3	14.3	16.9
Sample 3	14.5	14.4	18.2

4. Results and discussion

4.1. Physical defects

This section discusses the results related to sintering shrinkage, experimental measurements of porosity, the distribution of porosity considered in the numerical model and the evaluation of the suitable mapping method. Concerning the shrinkage, the assessment and control was performed using calliper measurements of the 3D objects in the principal orientations before and after the debinding and sintering stage. The dimensional difference between a green part and a sintered part can be seen in Fig. 7. All samples were sintered in the same position and presented identical geometrical shrinkage values in the XY plane, i.e. around 14.5%. However, the shrinkage in Z axis typically has a greater variation, studies show that shrinkage on the samples depends on their features [41]. Even so, this variation is most likely to also have occur due to the presence of delamination defects that increase the volume of the samples on the Z axis. The results of the shrinkage are presented in Table 3.

In Fig. 8 it is presented the porosity distribution within the specimen evaluated by μXCT. Both the shaping and debinding stages generated some porosity in the specimen. The large pores were created due to the increasing pressure applied by the trapped gas, which resulted from decomposed binder and additives. The delamination debinding defect present in the gauge section of the specimen has 2.18 mm^3 of volume and it is roughly on the same layer as the majority of shaping defects (see side view of the highlighted zone in Fig. 8). Thus, this zone was prone to gas accumulation, leading to large delamination. The shaping elongated defects were caused by insufficient extrusion multiplier during the shaping phase. Indeed, the porosity pattern is similar to the rectilinear parameter of infill (see Fig. 1 (b)). The side view shows that the defects present in the specimen are heterogeneously distributed through the thickness.

The total volume of the voids detected in the μXCT analysis is 21.83 mm^3, while the scanned specimen volume is 672.57 mm^3, i.e. there is 3.14% porosity detected. This value is in agreement with values found in the literature for specimens manufactured by MEX [55]. Fig. 9 presents the relationship between diameter (maximum permissible diameter of a

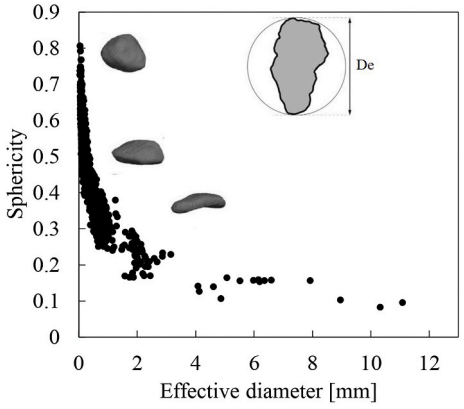

Fig. 9. Relationship between the maximum permissible diameter of a defect and sphericity of the detected pores.

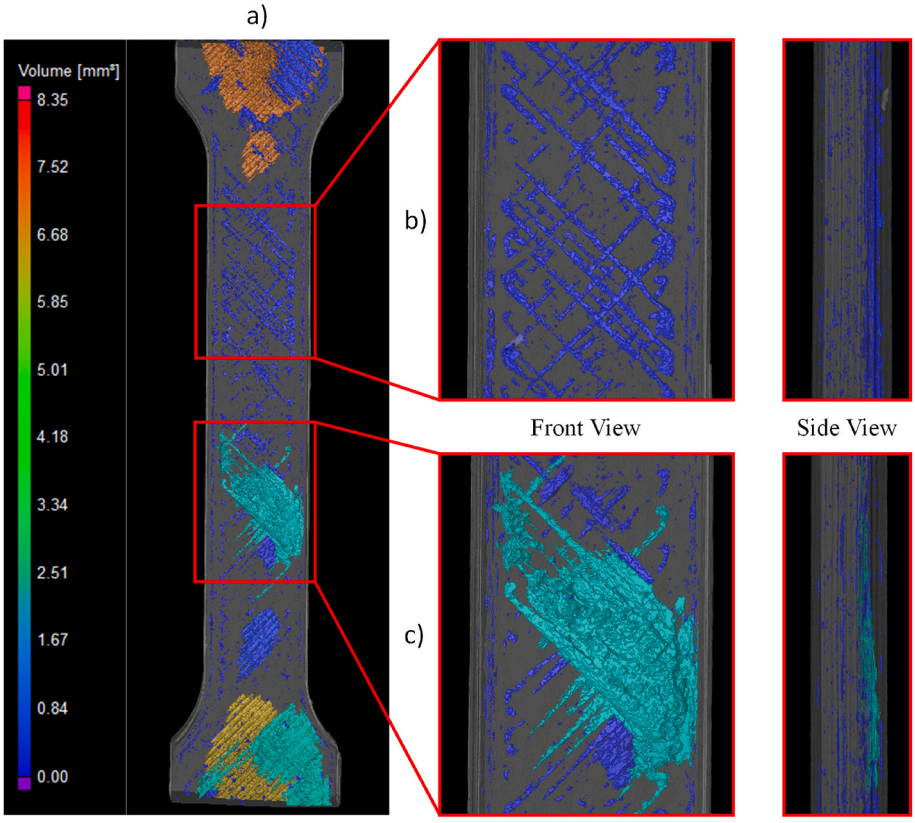

Fig. 8. a) μXCT dimensional results of specimen 3: Size, location and shape of porosity; b) front and side view of the zone highlighted showing the presence of elongated porosity; c) front and side view of the second highlighted zone showing the presence of a delamination defect.

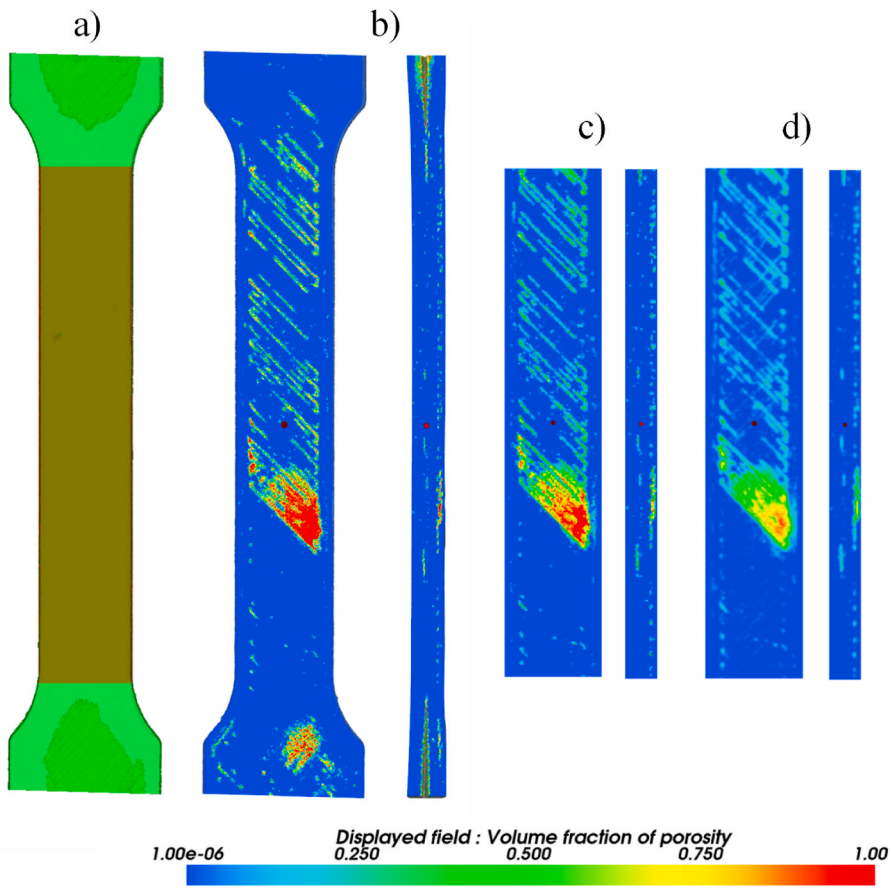

Fig. 10. a) 3D object space transformation: automatic superposition of donor and receiver volumes. b) Distributed volume fraction of porosity in the donor mesh. c) Volume fraction of porosity of the FE receiver mesh with ELE2INT mapping method. d) Volume fraction of porosity of the FE receiver mesh with INT-NODE2INT mapping method.

defect) and sphericity of the voids detected in the μXCT analysis. The largest pores caused by debinding delamination and insufficient extrusion have a very elongated shape (small sphericity). On the other hand, 67.4 % of the pores are small in size and present a sphericity value equal or larger than 0.5.

To consider the impact of the physical defects on the overall mechanical performance of the 3D object it is necessary to include the data of the detected porosity in the numerical modelling of the uniaxial tensile test. Hence, Fig. 10 (a) presents the automatic superposition of both donor and receiver meshes. The mapping of the porosity distribution from the donor mesh (see Fig. 10 (b)) to the receiving mesh is presented in Fig. 10 (c)–(d) using two different mapping methods. The results are displayed using the geometry's front and side cut views, wherein it is possible to identify interior zones with higher values of

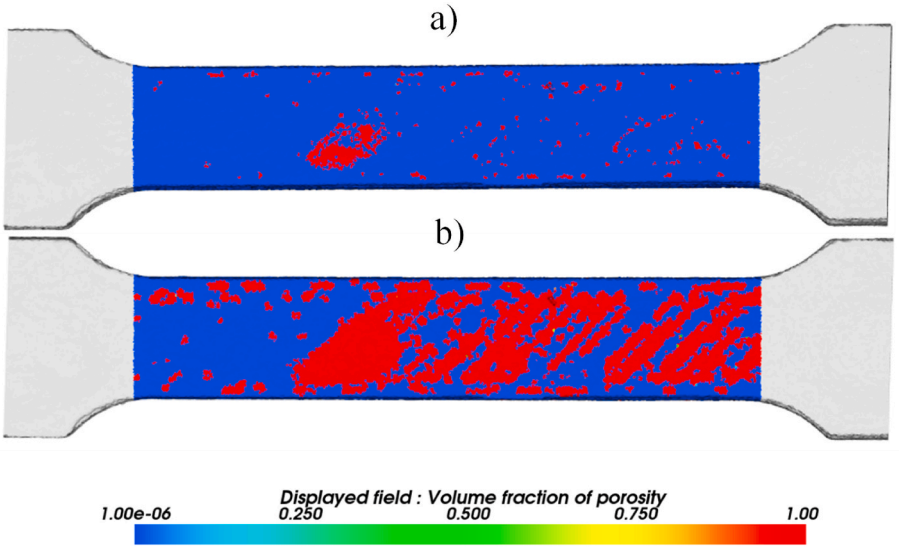

Fig. 11. Porosity data mapping relative error: a) ELE2INT. b) INT-NODE2INT.

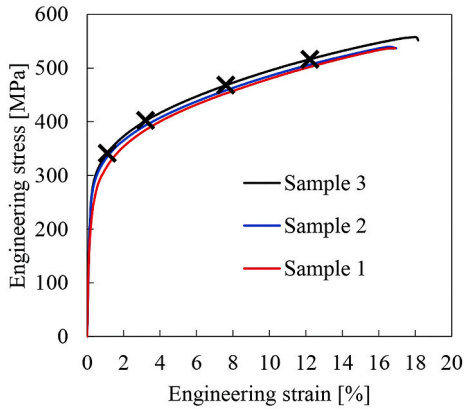

Fig. 12. Evaluation of the engineering stress-strain evolution in three samples obtained by MEX. Marks on the curve identify instants for experimental and numerical strain distribution measurement (1.1%, 3.2%, 7.6% and 12.2% engineering strain measured with virtual extensometer).

volume fraction of porosity (delamination defect). The results show that the ELE2INT mapping method proved to be a more effective method to map the volume fraction of porosity. The difference between the mapped porosity distribution and the porosity distribution defined in the donor mesh was lower using the ELE2INT (Fig. 10 (c)), than with the INT-NODE2INT method (Fig. 10 (d)). Indeed, the INT-NODE2INT method produced a smoothing on the mapped volume fraction of porosity (from 0.990 to 0.923), as shown in Fig. 10 (d). Therefore, only the ELE2INT mapping method was considered in the definition of the porosity distribution used in in the structural simulation. In mapping procedure, both the donor and receiver mesh have the minimum value of porosity assumed for each FE defined as 10^{-6}.

The performance of each mapping method can be evaluated using an error indicator. The relative error in each finite element can be defined as the difference between the porosity volume fraction defined in the initial donor mesh and the porosity mapped back to the donor mesh after being mapped to the receiving mesh (reversed mapping). Fig. 11 presents the absolute value of the relative error of each mapping method adopted. The number of finite elements with different porosity volume fraction after the reverse mapping is larger using the INT-NODE2INT method. Thus, the relative error indicator is another prove that the ELE2INT is a more accurate method. Concerning the mapping method used in the FE analysis (ELE2INT), the small difference in the porosity volume fraction is affected by the differences between donor and receiver mesh refinement.

4.2. Experimental strength

The mechanical strength of the samples fabricated by MEX was evaluated by carrying out uniaxial tensile tests and the engineering stress-strain curves are presented in Fig. 12. The strain in the gauge area was evaluated by the DIC system using a virtual extensometer placed at

Table 4
Comparison of the average tensile test results with other flat printed SS316L specimens.

Source	Young modulus (GPa)	σ_y 0,2% (MPa)	UTS (MPa)	Elongation at break (%)
Present study	164.9 (±12.7)	231.3 (±22.1)	545 (±11.35)	17.3 (±0.7)
Pellegrini et al. [10]	143.9–182.8	106.7–125.7	387.7–405.2	38–45
Caminero et al. [9]	151.3	179.9	497.1	36.7
Kurose et al. [11]	–	–	450	48
Sandvik (as sintered) [57]	160 (±20)	200 (±5)	500 (±15)	60 (±3)

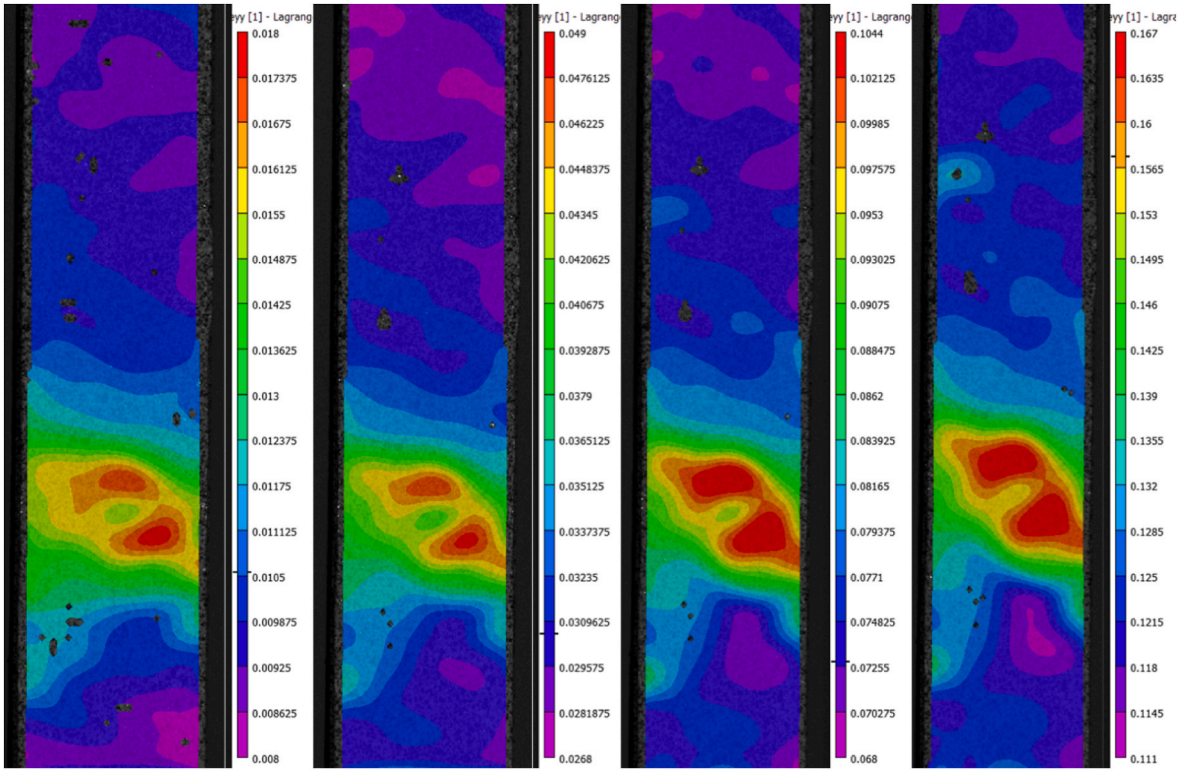

Fig. 13. Distribution of localized strains for 1.1%, 3.2%, 7.6% and 12% overall engineering strain.

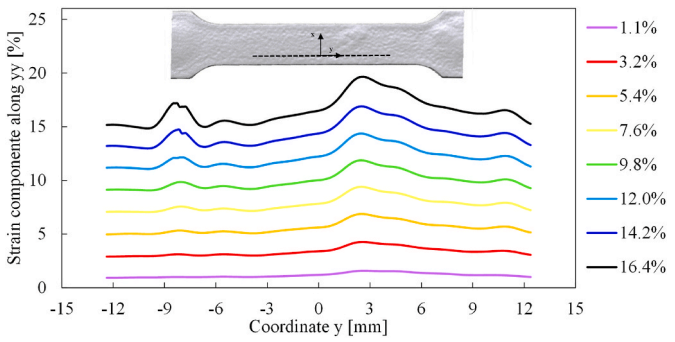

Fig. 14. Evolution of distribution of strains extracted in the line highlighted in black for different values of overall engineering tensile test strain.

middle of the specimen (23 mm of initial gauge length). Although there is the presence of internal porosity defects, the uniaxial tensile tests reproducibility was very high. The average mechanical properties resulting from the three samples are presented in Table 4, namely the Young modulus (E), the yield stress (σ_y), the ultimate tensile stress (UTS) and the elongation at break (e). The obtained results are compared with other literature results in order to validate the MEX sample preparation. Since the parts produced by MEX technology have anisotropic mechanical properties, i.e, depending on the build orientation, the comparison was conducted only with the studies where specimens were printed in the flat orientation [9,11]. The present samples show higher values of yield stress and ultimate tensile stress in comparison with the literature and material (powder) supplier values as it is shown in Table 4. Although it is proven that elongation at fracture reduces with the increase in porosity [13,18], the difference between these results and those published in the literature could be related to sintering and post-sintering conditions, since the formation of precipitates significantly affect the ductility [12,56].

The strain field in the gauge area measured in four different instants during the uniaxial tensile test is presented in Fig. 13 (identified in Fig. 12 with a cross symbol). The highest strain value arises in the debinding delamination pore zone, highlighted in the detailed view of Fig. 8 (c). The range of the strain field at the last instant shows deformations between 11.1% and 16.7%, corresponding to 12.2% of overall engineering strain measured with the virtual extensometer. Therefore, the internal porosity yields this heterogeneity of the strain field in the gauge area.

The regions with larger strain values are always located in the same region during the loading (see Fig. 13), i.e., the region containing the debinding delamination defect pore. Globally, the strain in the gauge area is increasing during the loading.

Fig. 14 shows the evolution of the strain distribution (component along the loading direction) measured along a straight line, located on the specimen gauge area. The strain is not uniform along the line, presenting two zones of strain concentration, fixed during the entire uniaxial tensile test. The region showing the largest value of strain is located in the debinding defect, about 3 mm of y coordinate. The second zone with the highest strains is located around −8 mm of y coordinate, as shown in Fig. 14. Although this zone does not contain the maximum strain value, the strain gradient is larger in this location, particularly for large loading values. Indeed, the final failure of the specimen occurs in the cross section containing this zone. Fig. 15 (a) presents the tensile specimen after fracture, which was prepared for DIC analysis.

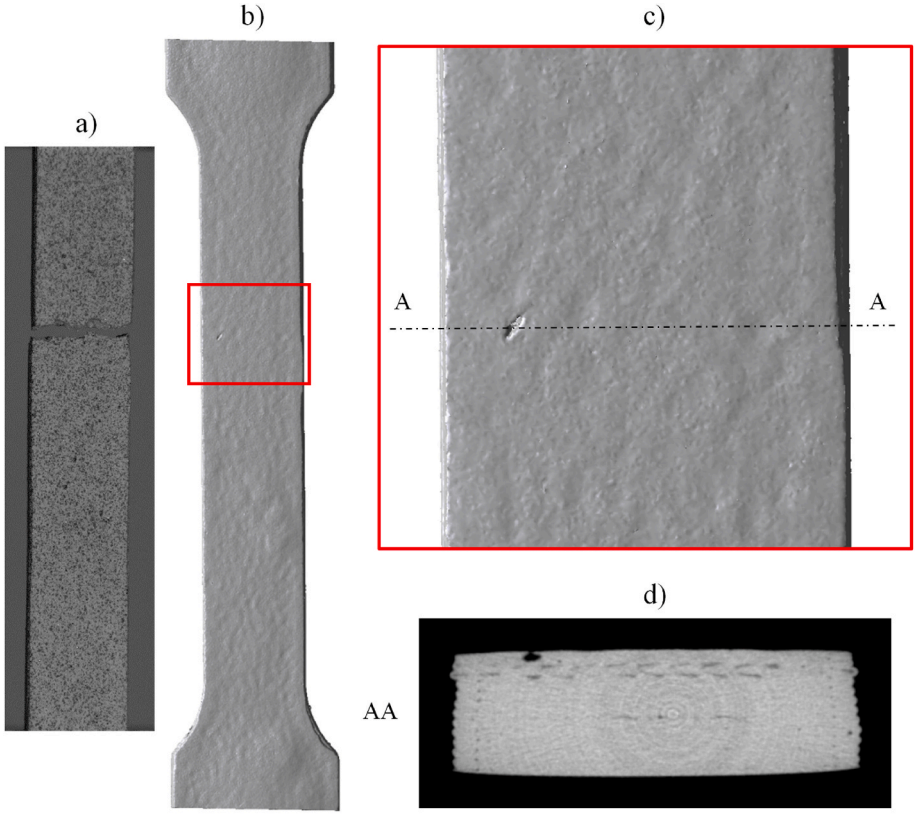

Fig. 15. a) DIC photo after the moment of test failure showing spray painted specimen 3 and fracture location; b) Surface reconstruction of the specimen 3 showing surface defect in the zone highlighted in red (fracture location); c) close up view of the surface defect that led to test failure; d) μXCT section cut (AA) view displayed in c) showing the presence of internal porosity near the surface defect location. (For interpretation of the references to colour in this figure legend, the reader is referred to the Web version of this article.)

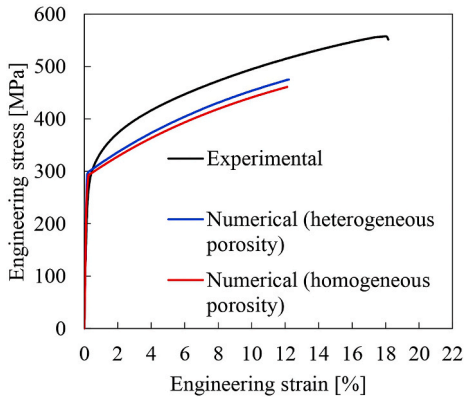

Fig. 16. Comparison of the engineering stress and strain of the uniaxial tensile test for specimen three, the multi-scale method and the model with homogeneous porosity distribution.

Fig. 15 (b) present the initial geometry of the specimen (prior to the uniaxial tensile test) obtained by μXCT. The specimen adopted in the uniaxial tensile test presents a surface defect near the zone with the larger strain gradient. Fig. 15 (c) and (d) show a detail view of this defect, which is visible either from the exterior surface of the specimen or the cross-section obtained by μXCT analysis. The dimensions of this defect are approximately 0.69 mm and 0.2 mm in length and width respectively. This defect may have been created in the shaping phase of the MEX process, comprising the first layer deposition. Other possible causes for the origin of the surface defect could be because of a contamination of a second phase particle that was degraded in the debinding and sintering or due to small inhomogeneity in the mixture.

4.3. Numerical analysis

The finite element predictions were obtained considering two different numerical models. The first model uses the mapping method ELE2INT to assign the μXCT measured porosity distribution to the finite element mesh. On the other hand, the second model considers a uniform distribution of the porosity (3.14%) in the finite element analysis. The constitutive material model is identical in both simulations. The displacement of two predefined nodes was assessed during the uniaxial tensile test, replicating the virtual extensometer conditions used in the DIC, and allowing the comparison of the numerical and experimental measurements.

Fig. 16 compares the experimental stress-strain evolution for both predictions (homogeneous and heterogeneous porosity distributions). The predicted mechanical strength of the specimen is underestimated, particularly when the homogeneous porosity distribution is used in the numerical model. This difference can be a consequence of several factors. The material is assumed isotropic (von Mises) in the numerical model, the adopted hardening law is relatively simple and the material parameters were calibrated using the experimental stress–strain curve obtained by Cooper et al. [46] for a sintered material. Besides, the mapped porosity distribution used in the numerical model is affected by the accuracy of the μXCT.

Since the post-processing results of the VIC-3D software are related

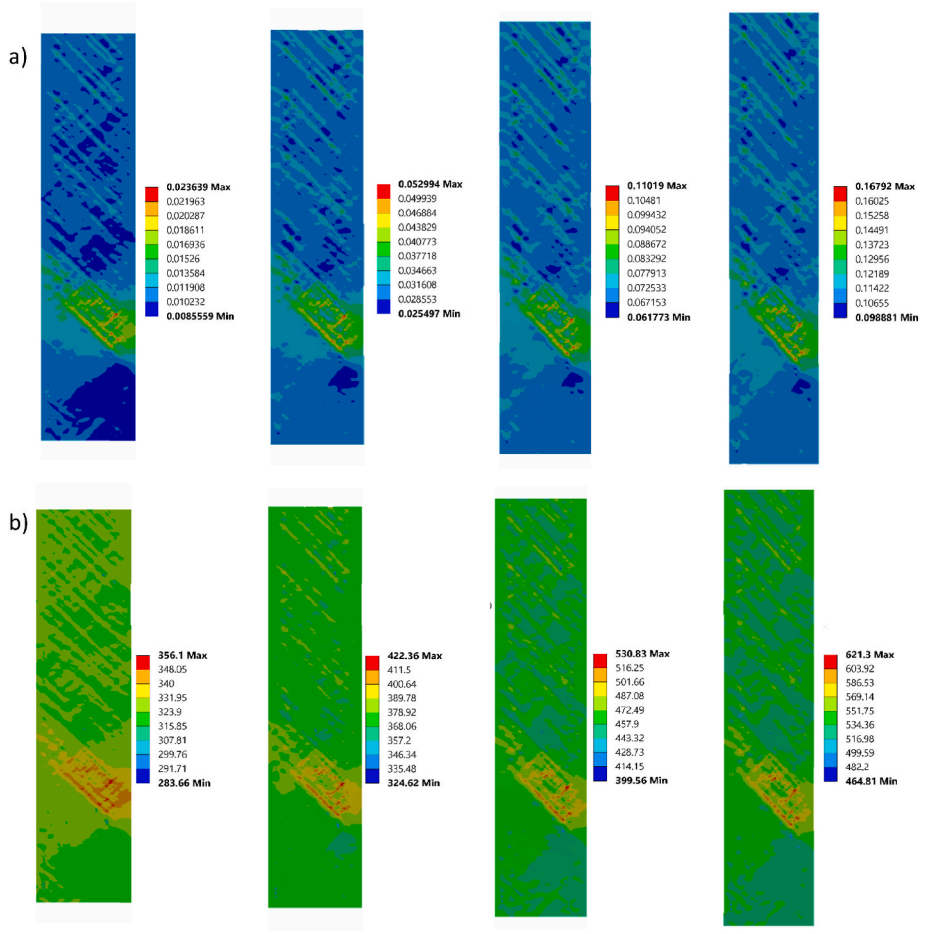

Fig. 17. Multi-scale model results at four marked points (1.1%, 3.2%, 7.6% and 12% overall engineering strain): a) Strains distribution field; b) Stress distribution field.

to a 2D strain field within a region of interest, the simulation results are also presented for the same region of interest (yy = 28 mm). Hence, Fig. 17 (a) presents the strain field's evolution in the specimen's gauge area predicted by the model that considers a heterogeneous porosity distribution. The contour fields of strain values are displayed for 1.1%, 3.2%, 7.6% and 12.2% of strain in the virtual extensometer (the four instants identified in Fig. 12). The maximum strain value arises in the debinding delamination defect zone. The predicted strain distribution aligns globally with the experimental measurements (Fig. 13).

Moreover, the porosity distribution adopted in the numerical model (see Fig. 10 (c)) directly impacts the obtained strain field. Indeed, the predicted strain values are larger in the zones with large porosity. Considering the last instant evaluated, the maximum and minimum strain values in the specimen predicted by the model with heterogeneous porosity distribution were 16.8% and 9.9% respectively. Therefore, comparing the numerical prediction (Fig. 17 (a)) with the experimental measurement (Fig. 13) allows to conclude the high level of accuracy of the numerical model with a variation of 0.53 % and 10.92 % for maximum and minimum stain values respectively. Nevertheless, the strain distribution evaluated by the VIC-3D system (averaged value within the facet area) seems smoother than the numerical field.

Fig. 17 (b) presents the distribution of von Mises stress predicted by the model using the heterogeneous porosity distribution, comparing the four different instants. The maximum values of true stress predicted by the model are located around the debinding delamination defect. In the last instant, the von Mises stress is 621.3 MPa in some concentrated regions, which is significantly larger than the uniform stress predicted by the uniform porosity distribution model (516 MPa).

To identify the zones where the model qualitatively had lower accuracy in predicting the distributions of the local strain, a lower independent value was added to the lower strain values in the band scale, represented in Fig. 18. The scale modification allows the identification

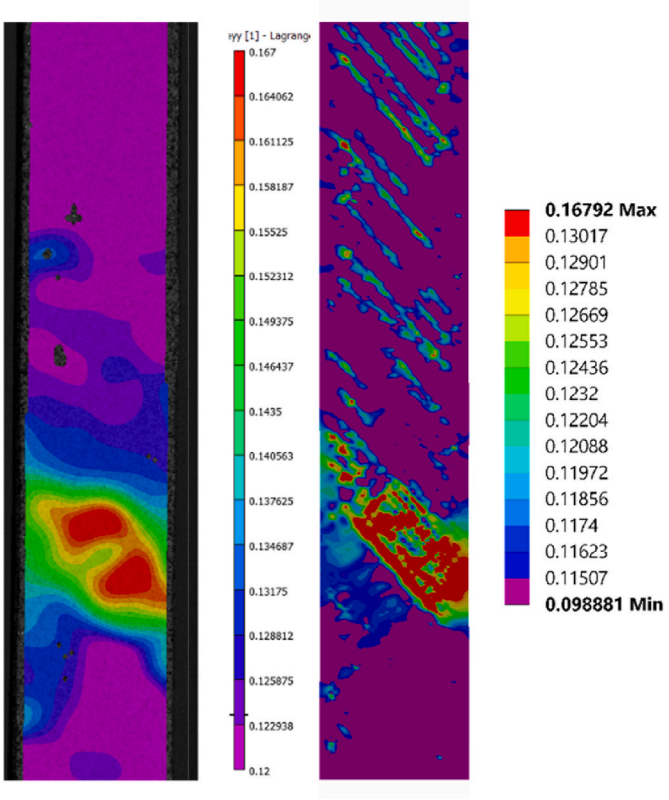

Fig. 18. Strain comparison (DIC vs Multi-scale model) for 12.2% overall engineering strain with a lower independent band to highlight the zones with different high values of strain.

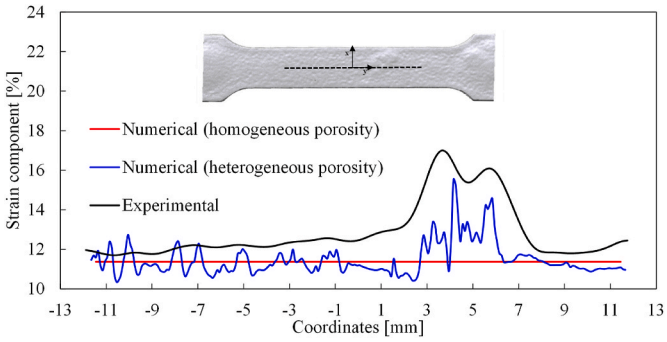

Fig. 19. Strain distribution outputted over a centre line for 12.2% of engineering strain. Image correlation vs numerical model with heterogeneous porosity (blue) vs numerical model with homogeneous porosity (red). (For interpretation of the references to colour in this figure legend, the reader is referred to the Web version of this article.)

of the consequence of shaping defects on the numeric results, present along the strand printed line (45°) and the morphology of the strain distribution in the debinding delamination defect. The model generally shows good accuracy in predicting strain localization and magnitude. The difference could be attributed to the VIC-3D correlation smoothing of strain distributions, while the numerical model smoothes the outputs of the strain results of the element integration points over to the nodes. The mapping scatter error could also influence the final results; the results would undoubtedly be more accurate given a similar mesh mapping or a mapping procedure without scatter errors. Failure could not be predicted with the model as the surface defects are not considered pores, so they weren't mapped to the final 3D simulation mesh. Additionally, the surface defect was not discretized geometrically.

The experimental and numerical strain distribution was compared at the simulation's end (last instant defined in Fig. 12), considering a straight line (~25 mm of length) located in the middle of the specimen gauge area. The comparison is presented in Fig. 19, considering both numerical models: homogeneous and heterogeneous porosity distribution. Only the numerical model that considers the real porosity distribution inside the specimen can accurately predict the strain distribution measured experimentally. However, the finite element model slightly under predicts the experimental strain distribution. The differences can be due to smoothing associated with the DIC technique, the error during the mapping of the porosity distribution to the mesh used in the FE analysis and the material properties used to describe the behaviour of the material.

Nevertheless, the proposed model could have an important and significant impact on the qualification of MAM components, being able to predict mechanical structural performance without destroying specimens and decreasing the rate of false rejections. The model showed a close prediction of mechanical properties overall and could be used not only to study the load capacity but also to predict failure location and fatigue life with strain-based methods.

5. Conclusions

MAM technologies generally result in complex geometries with a pervasive presence of porosity in their microstructures, varying in size, shape, and distribution. These pore defects impact the overall structure load capacity and life of metal components. This study presents a novel methodology to predict and qualify MAM components with specific microstructures. Using the capability of dimensional control of μXCT and multi-scale simulation to predict the influence of all the pores detected in mechanical structural performance. The multi-scale model doesn't have the limitation of discretization, being able to account for every pore detected in the μXCT dimensional analysis. The following conclusions can be drawn with this study:

1. Optimizing the shape, debinding and sinter parameters is essential to produce final metal parts with low porosity. With the μXCT analysis it was possible to conclude that the final microstructure had several types of pores, varying in shape, dimension and location. The major defects formed in the shaping phase had elongated shape and followed the strand printing line, while the debinding defects manifested in the form of blisters. Despite the pores, all the test specimens had reproducibility and all three tests had consistent results, almost in the same range of those found in the literature.
2. DIC analysis made possible to evaluate the impact of defect microstructure in the strain evolution and concentration during a uniaxial tensile test. The microstructure defects largely affect the concentration of strains, with specimen three showcasing the higher strain deformation on the zone of the debinding delamination defect. Even though the highest amount of strain was located in the blister zone, the mechanical failure occurred due to a surface defect. The combination of the tortuous shape's surface defect and the nearby presence of internal porosity led to the sudden structural failure.
3. Element to integration point (ELE2INT) is a superior mapping method to this case than the Integration point-node to integration point (INT-NODE2INT). Despite the meshes not being similar, Digimat-MAP provided a good bridge to map microstructural metrological analysis to the numerical simulation platform.
4. Multi-scale simulation was able to consider the microstructure pore defects in the mechanical structural analysis with success. The multi-scale model predicted the higher concentration of strains in the dedinding delamination defect and had an overall close distribution of strains in the analysed face compared with VIC correlation results. The differences between the model and the real analysis could be due to the small scatter of porosity volume fraction mapping error and the initial material model used in Digimat-MF. Regardless, the study showed good first approximation to the problem.
5. The open potential for qualification of MAM components as a non-destructive test methodology is real, as it could improve the quality control of components with pores.

In the future, several studies could be carried out to improve the precision and validation of the multi-scale model. A digital volume correlation, using interrupted uniaxial tensile test with in-situ μXCT could be used to compare the strains at the surface and all over the component 3D volume. In the case of MEX, a model of predicting the final metal part pore microstructure after sintering could be coupled via mapping to predict the final structural metal part performance and avoid spending energy sintering unwanted 3D green objects.

CRediT authorship contribution statement

L.M. Cacho: Conceptualization, Methodology, Validation, Formal analysis, Investigation, Data curation, Writing – original draft, Visualization. **M.A. Neto:** Investigation, Data curation, Writing – review & editing, Visualization, Supervision. **D.M. Neto:** Investigation, Data curation, Writing – review & editing, Visualization, Supervision. **M.T. Vieira:** Conceptualization, Resources, Supervision, Funding acquisition.

Declaration of competing interest

The authors declare that they have no known competing financial interests or personal relationships that could have appeared to influence the work reported in this paper.

Acknowledgements

This research is financed by PRR - Recovery and Resilience Plan and by the Next Generation EU Funds, following NOTICE N. ° 02/C05-i01/2022, Component 5 – Capitalization and Business Innovation - Mobilizing Agendas for Business Innovation under the INOV.AM project "Innovation in Additive Manufacturing" (reference: C628518748–00464029 | 7999). This research is sponsored by national funds through FCT – Fundação para a Ciência e a Tecnologia, under the project UIDB/00285/2020 and LA/P/0112/2020.

References

[1] ISO/ASTM52900-15. Standard Terminology for additive manufacturing – general principles – terminology (ASTM52900). Int. Organ. Stand. Geneva 2015;Switz. i: 1–9.
[2] Turner BN, Strong R, Gold SA. A review of melt extrusion additive manufacturing processes: I. Process design and modeling. Rapid Prototyp J 2014;20:192–204. https://doi.org/10.1108/RPJ-01-2013-0012.
[3] Suwanpreecha C, Manonukul A. A review on material extrusion additive manufacturing of metal and how it compares with metal injection moulding. Metals 2022;12:429. https://doi.org/10.3390/met12030429.
[4] Deckers J, Vleugels J, Kruth JP. Additive manufacturing of ceramics: a review. J Ceram Sci Technol 2014;5:245–60. https://doi.org/10.4416/JCST2014-00032.
[5] Armstrong M, Mehrabi H, Naveed N. An overview of modern metal additive manufacturing technology. J Manuf Process 2022;84:1001–29. https://doi.org/10.1016/j.jmapro.2022.10.060.
[6] Gonzalez-Gutierrez J, Godec D, Kukla C, Schlauf T, Burkhardt C, Holzer Gonzalez-Gutierrez CJ, Leoben M, Glöckel-Straße O, Ass Godec LD, Kukla mont C, Schlauf IT, Burkhardt PC, Holzer PC. Shaping, debinding and sintering of steel components via fused filament fabrication. In: 16 Th Int. Sci. Conf. Prod. Eng.; 2017. p. 8–10.
[7] Lotfizarei Z, Mostafapour A, Barari A, Jalili A, Patterson AE. Overview of debinding methods for parts manufactured using powder material extrusion. Addit Manuf 2023;61:103335. https://doi.org/10.1016/j.addma.2022.103335.
[8] Thompson Y, Gonzalez-Gutierrez J, Kukla C, Felfer P. Fused filament fabrication, debinding and sintering as a low cost additive manufacturing method of 316L stainless steel. Addit Manuf 2019;30:100861. https://doi.org/10.1016/j.addma.2019.100861.
[9] Caminero MÁ, Romero A, Chacón JM, Núñez PJ, García-Plaza E, Rodríguez GP. Additive manufacturing of 316L stainless-steel structures using fused filament fabrication technology: mechanical and geometric properties. Rapid Prototyp J 2021;27:583–91. https://doi.org/10.1108/RPJ-06-2020-0120.
[10] Pellegrini A, Palmieri ME, Guerra MG. Evaluation of anisotropic mechanical behaviour of 316L parts realized by metal fused filament fabrication using digital image correlation. Int J Adv Manuf Technol 2022;120:7951–65. https://doi.org/10.1007/s00170-022-09303-z.
[11] Kurose T, Abe Y, Santos MVA, Kanaya Y, Ishigami A, Tanaka S, Ito H. Influence of the layer directions on the properties of 316L stainless steel parts fabricated through fused deposition of metals. Materials 2020;13:2493. https://doi.org/10.3390/ma13112493.
[12] Wagner MA, Engel J, Hadian A, Clemens F, Rodriguez-Arbaizar M, Carreño-Morelli E, Wheeler JM, Spolenak R. Filament extrusion-based additive manufacturing of 316L stainless steel: effects of sintering conditions on the microstructure and mechanical properties. Addit Manuf 2022;59:103147. https://doi.org/10.1016/j.addma.2022.103147.
[13] Meng LX, Ben DD, Yang HJ, Ji HB, Lian DL, Zhu YK, Chen J, Yi JL, Wang L, Yang JB, Zhang ZF. Effects of embedded spherical pore on the tensile properties of a selective laser melted Ti6Al4V alloy. Mater Sci Eng 2021;815:141254. https://doi.org/10.1016/j.msea.2021.141254.
[14] Falkowska A, Seweryn A, Tomczyk A. Fatigue life and strength of 316L sintered steel of varying porosity. Int J Fatig 2018;111:161–76. https://doi.org/10.1016/j.ijfatigue.2018.02.023.
[15] Carlton HD, Haboub A, Gallegos GF, Parkinson DY, MacDowell AA. Damage evolution and failure mechanisms in additively manufactured stainless steel. Mater Sci Eng 2016;651:406–14. https://doi.org/10.1016/j.msea.2015.10.073.
[16] Beretta S, Romano S. A comparison of fatigue strength sensitivity to defects for materials manufactured by AM or traditional processes. Int J Fatig 2017;94:178–91. https://doi.org/10.1016/j.ijfatigue.2016.06.020.
[17] du Plessis A, Yadroitsava I, Yadroitsev I. Effects of defects on mechanical properties in metal additive manufacturing: a review focusing on X-ray tomography insights. Mater Des 2020;187:108385. https://doi.org/10.1016/j.matdes.2019.108385.
[18] Wilson-Heid AE, Novak TC, Beese AM. Characterization of the effects of internal pores on tensile properties of additively manufactured Austenitic stainless steel 316L. Exp Mech 2019;59:793–804. https://doi.org/10.1007/s11340-018-00465-0.
[19] Miers JC. Deformation and failure of additively manufactured ductile metals with internal porosity. Georgia Institute of Technology; 2021.
[20] Vafadar A, Guzzomi F, Rassau A, Hayward K. Advances in metal additive manufacturing: a review of common processes, industrial applications, and current challenges. Appl Sci 2021;11:1213. https://doi.org/10.3390/app11031213.
[21] Altıparmak SC, Yardley VA, Shi Z, Lin J. Challenges in additive manufacturing of high-strength aluminium alloys and current developments in hybrid additive manufacturing. Int. J. Light. Mater. Manuf. 2021;4:246–61. https://doi.org/10.1016/j.ijlmm.2020.12.004.
[22] Thijs L, Verhaeghe F, Craeghs T, Van Humbeeck J, Kruth J-P. A study of the microstructural evolution during selective laser melting of Ti–6Al–4V. Acta Mater 2010;58:3303–12. https://doi.org/10.1016/j.actamat.2010.02.004.
[23] Hardin RA, Beckermann C. Effect of porosity on deformation, damage, and fracture of cast steel. Metall Mater Trans 2013;44:5316–32. https://doi.org/10.1007/s11661-013-1669-z.

[24] Jedrychowski M, Garner SA, Arnau Izquierdo G. Comparison of X-ray computed tomography and immersion ultrasonic non-destructive testing techniques in the case of qualitative and quantitative assessment of brazing quality level. E-Journal Nondestruct. Test. 2019;24:1–8. https://doi.org/10.58286/23671.
[25] Amthe OM, Industry T, Control Q, Ct WX. Metal AM - the magazine for the metal. Additive Manufacturing Industry 2017;3:132.
[26] Liverani E, Fortunato A. Additive manufacturing of AISI 420 stainless steel: process validation, defect analysis and mechanical characterization in different process and post-process conditions. Int J Adv Manuf Technol 2021;117:809–21. https://doi.org/10.1007/s00170-021-07639-6.
[27] Okuma G, Watanabe S, Shinobe K, Nishiyama N, Takeuchi A, Uesugi K, Tanaka S, Wakai F. 3D multiscale-imaging of processing-induced defects formed during sintering of hierarchical powder packings. Sci Rep 2019;9:11595. https://doi.org/10.1038/s41598-019-48127-y.
[28] Kim FH, Moylan SP, Garboczi EJ, Slotwinski JA. Investigation of pore structure in cobalt chrome additively manufactured parts using X-ray computed tomography and three-dimensional image analysis. Addit Manuf 2017;17:23–38. https://doi.org/10.1016/j.addma.2017.06.011.
[29] Senck S, Happl M, Reiter M, Scheerer M, Kendel M, Glinz J, Kastner J. Additive manufacturing and non-destructive testing of topology-optimised aluminium components, Nondestruct. Test. Eval 2020;35:315–27. https://doi.org/10.1080/10589759.2020.1774582.
[30] Afazov S, Roberts A, Wright L, Jadhav P, Holloway A, Basoalto H, Milne K, Brierley N. Metal powder bed fusion process chains: an overview of modelling techniques. Prog. Addit. Manuf. 2022;7:289–314. https://doi.org/10.1007/s40964-021-00230-1.
[31] Panwisawas C, Qiu C, Anderson MJ, Sovani Y, Turner RP, Attallah MM, Brooks JW, Basoalto HC. Mesoscale modelling of selective laser melting: thermal fluid dynamics and microstructural evolution. Comput Mater Sci 2017;126:479–90. https://doi.org/10.1016/J.COMMATSCI.2016.10.011.
[32] Siddique S, Imran M, Rauer M, Kaloudis M, Wycisk E, Emmelmann C, Walther F. Computed tomography for characterization of fatigue performance of selective laser melted parts. Mater Des 2015;83:661–9. https://doi.org/10.1016/j.matdes.2015.06.063.
[33] Kim FH, Moylan SP, Phan TQ, Garboczi EJ. Investigation of the effect of artificial internal defects on the tensile behavior of laser powder bed fusion 17–4 stainless steel samples: simultaneous tensile testing and X-ray computed tomography. Exp Mech 2020;60:987–1004. https://doi.org/10.1007/s11340-020-00604-6.
[34] du Plessis A, Yadroitsava I, le Roux SG, Yadroitsev I, Fieres J, Reinhart C, Rossouw P. Prediction of mechanical performance of Ti6Al4V cast alloy based on microCT-based load simulation. J Alloys Compd 2017;724:267–74. https://doi.org/10.1016/j.jallcom.2017.06.320.
[35] Hamid M, Saleh MS, Afrouzian A, Panat R, Zbib HM. Modeling of porosity and grain size effects on mechanical behavior of additively manufactured structures. Addit Manuf 2021;38:101833. https://doi.org/10.1016/j.addma.2020.101833.
[36] Darabi R, Azinpour E, Fiorentin FK, Abarca MJ, Cesar de Sá J, Dzugan J. Experimental and computational analysis of additively manufactured tensile specimens: assessment of localized-cooling rate and ductile fracture using the Gurson– Tvergaard–Needleman damage model. Proc Inst Mech Eng Part L J Mater Des Appl 2021;235:1430–42. https://doi.org/10.1177/1464420721990049.
[37] Xin S, Zhang L, Chen M, Gebhardt C, Chen G. Understanding influence of micro pores on strengths of LMDed AlSi10Mg material using a direct method based statistical multiscale framework. Mater Des 2022;214:110409. https://doi.org/10.1016/j.matdes.2022.110409.
[38] Doroszko M, Seweryn A. A new numerical modelling method for deformation behaviour of metallic porous materials using X-ray computed microtomography. Mater Sci Eng 2017;689:142–56. https://doi.org/10.1016/j.msea.2017.02.055.
[39] Meng LX, Ben DD, Yang HJ, Ji HB, Lian DL, Zhu YK, Chen J, Yi JL, Wang L, Yang JB, Zhang ZF. Effects of embedded spherical pore on the tensile properties of a selective laser melted Ti6Al4V alloy. Mater Sci Eng 2021;815:141254. https://doi.org/10.1016/j.msea.2021.141254.
[40] Cerejo F, Gatões D, Vieira MT. Optimization of metallic powder filaments for additive manufacturing extrusion (MEX). Int J Adv Manuf Technol 2021;115:2449–64. https://doi.org/10.1007/s00170-021-07043-0.
[41] Gong H, Snelling D, Kardel K, Carrano A. Comparison of stainless steel 316L parts made by FDM- and SLM-based additive manufacturing processes. JOM 2019;71:880–5. https://doi.org/10.1007/s11837-018-3207-3.
[42] ASTM E8. ASTM E8/E8M standard test methods for tension testing of metallic materials 1. Annu. B. ASTM Stand. 2010;4:1–27. https://doi.org/10.1520/E0008_E0008M-22.
[43] Ait-Mansour I, Kretzschmar N, Chekurov S, Salmi M, Rech J. Design-dependent shrinkage compensation modeling and mechanical property targeting of metal FFF. Prog. Addit. Manuf. 2020;5:51–7. https://doi.org/10.1007/s40964-020-00124-8.
[44] Tancogne-Dejean T, Roth CC, Mohr D. Rate-dependent strength and ductility of binder jetting 3D-printed stainless steel 316L: experiments and modeling. Int J Mech Sci 2021;207:106647. https://doi.org/10.1016/j.ijmecsci.2021.106647.
[45] MSC Sofware Belgiumm SA. Digimat user manual, vol. 2. Release; 2021. p. 2021.
[46] Cooper AJ, Brayshaw WJ, Sherry AH. Tensile fracture behavior of 316L austenitic stainless steel manufactured by hot isostatic pressing. Metall Mater Trans 2018;49:1579–91. https://doi.org/10.1007/s11661-018-4518-2.
[47] Dasappa P, Inal K, Mishra R. The effects of anisotropic yield functions and their material parameters on prediction of forming limit diagrams. Int J Solid Struct 2012;49:3528–50. https://doi.org/10.1016/j.ijsolstr.2012.04.021.
[48] Mori T, Tanaka K. Average stress in matrix and average elastic energy of materials with misfitting inclusions. Acta Metall 1973;21:571–4. https://doi.org/10.1016/0001-6160(73)90064-3.
[49] Wu L, Noels L, Adam L, Doghri I. An implicit-gradient-enhanced incremental-secant mean-field homogenization scheme for elasto-plastic composites with damage. Int J Solid Struct 2013;50:3843–60. https://doi.org/10.1016/j.ijsolstr.2013.07.022.
[50] Sun X, Gao Z, Cao P, Zhou C. Mechanical properties tests and multiscale numerical simulations for basalt fiber reinforced concrete. Construct Build Mater 2019;202:58–72. https://doi.org/10.1016/j.conbuildmat.2019.01.018.
[51] Sachse R, Pickett AK, Middendorf P. Simulation of impact and residual strength of thick laminate composites. Composites Part B 2020;195:108070. https://doi.org/10.1016/j.compositesb.2020.108070.
[52] Sharafi S, Santare MH, Gerdes J, Advani SG. A multiscale modeling approach of the Fused Filament Fabrication process to predict the mechanical response of 3D printed parts. Addit Manuf 2022;51:102597. https://doi.org/10.1016/j.addma.2022.102597.
[53] Hu D, Shan Y, He T, Liu X, Wan X. Research on simulation method of impact resistance of composite wheels made of long glass fiber reinforced thermoplastic introducing anisotropic property. Compos Struct 2019;223:110965. https://doi.org/10.1016/j.compstruct.2019.110965.
[54] Hu D, Shan Y, He T, Liu X. Analysis on effect of injection residual stress on impact resistance of composite wheel made of long glass fiber reinforced thermoplastic. Int J Crashworthiness 2021;26:515–25. https://doi.org/10.1080/13588265.2020.1757583.
[55] Kedziora S, Decker T, Museyibov E, Morbach J, Hohmann S, Huwer A, Wahl M. Strength properties of 316L and 17-4 PH stainless steel produced with additive manufacturing. Materials 2022;15:6278. https://doi.org/10.3390/ma15186278.
[56] Sadaf M, Bragaglia M, Nanni F. A simple route for additive manufacturing of 316L stainless steel via Fused Filament Fabrication. J Manuf Process 2021;67:141–50. https://doi.org/10.1016/j.jmapro.2021.04.055.
[57] MetalPowder-Sandvik, (n.d.). https://www.metalpowder.sandvik/en/products/datasheets/austenitic-stainless-steel/osprey-316l/(accessed June 6, 2023).